Optics Letters

High-power single-frequency continuous-wave 355 nm UV laser via a frequency-correlated dual-wavelength laser

Jiao Wei,[1,2] Yongdong Wang,[1] Ruixi Yin,[1] Jing Su,[1,2] and Huadong Lu[1,2,*]

[1]State Key Laboratory of Quantum Optics and Quantum Optics Devices, Institute of Opto-Electronics, Shanxi University, Taiyuan 030006, China
[2]Collaborative Innovation Center of Extreme Optics, Shanxi University, Taiyuan 030006, China
*luhuadong@sxu.edu.cn

Received 10 May 2024; revised 30 June 2024; accepted 1 July 2024; posted 2 July 2024; published 12 July 2024

An all-solid-state single-frequency continuous-wave (CW) 355 nm ultraviolet (UV) laser based on a dispersion-compensated doubly resonant resonator is presented in this Letter that is achieved by employing homemade high-stability all-solid-state frequency-correlated dual-wavelength lasers at 1064 and 532 nm and a temperature-controlled type-I critical-phase-matching LiB_3O_5 (LBO) to act as the fundamental laser source and the nonlinear medium, respectively. The frequency-correlated dual-wavelength single-frequency CW laser supplies the fundamental frequency 1064 and 532 nm lasers with good frequency synchronization. And the temperature-controlled LBO acts as the dispersion-compensation element to realize double resonance of the 1064 and 532 nm laser. Finally, a 4.2 W high-stability 355 nm UV laser is experimentally obtained, and the corresponding total conversion efficiency is up to 20.5%. To the best of our knowledge, this is the highest power reported about single-frequency CW 355 nm UV laser. The presented method can pave a way to develop a compact single-frequency 355 nm UV laser with high output power. © 2024 Optica Publishing Group. All rights, including for text and data mining (TDM), Artificial Intelligence (AI) training, and similar technologies, are reserved.

https://doi.org/10.1364/OL.529817

All-solid-state single-frequency continuous-wave (CW) 355 nm ultraviolet (UV) laser sources have been widely applied in lots of fields including high-resolution spectroscopy [1], flow cytometry [2], and semiconductor inspection [3], owing to their intrinsic advantages of good mechanical stability, high single-photon energy, and perfect beam quality [4]. Especially, all-solid-state single-frequency CW 355 nm UV lasers have become popular candidates in the lithography field due to their high coherence and are gradually replacing the traditional argon lasers [5]. It is well-known that the all-solid-state CW 355 nm UV laser can be achieved based on sum-frequency generation between 1064 and 532 nm lasers [6]. As early as 1995, Sony Research Center [7] first obtained a single-frequency CW 355 nm UV laser by adopting an external doubly resonant sum-frequency cavity for 1064 and 532 nm lasers. However, the output power was limited to 186 mW because of the low incident powers of 1064 and 532 nm lasers. Moreover, the employed single-frequency CW 1064 and 532 nm lasers were from two individual Nd:YVO_4 lasers. In order to achieve the simultaneous resonance of two incident laser beams, the sum-frequency resonator had to be locked to the incident single-frequency 532 nm laser and the 1064 nm laser was locked to the oscillating frequency of the sum-frequency resonator, which made the 355 nm laser system complex. Based on the same experimental setup, the output power of the single-frequency 355 nm UV laser was further increased to 660 mW after the incident powers of the 1064 and 532 nm lasers were increased and the resonator structure was optimized [8]. In addition, some new nonlinear crystals including periodically poled stoichiometric Mg-doped $LiNbO_3$ (MgO:PPSLN) [9], periodically poled stoichiometric Mg-doped $LiTaO_3$ (MgO:PPSLT) [10], $La_2CaB_{10}O_{19}$ (LCBO) [11], and $Na_3La_9O_3(BO_3)_8$ (NLBO) [12] were manufactured and applied to generate the 355 nm UV laser. However, the output powers of the generated 355 nm UV laser were still limited to hundreds of mW level. In other words, there is not a single-frequency CW 355 nm UV laser with the output power over 1 W so far.

In this Letter, a high-stability single-frequency CW 355 nm laser with an output power of 4.2 W based on a dispersion-compensated double resonance-enhanced cavity is reported. Especially, a temperature-controlled type-I critical-phase-matching LBO is employed as the nonlinear medium as well as the dispersion compensation element. At the same time, it is worth mentioning that a homemade single-frequency CW dual-wavelength laser with output powers over 10 W plays an important role in the experiment because it can provide frequency-correlated fundamental 1064 and 532 nm lasers for the sum-frequency process. In this case, if only the sum-frequency resonator is locked to the incident 1064 nm laser, the simultaneous oscillation of the 532 nm laser can be realized after the dispersion compensation is achieved by controlling the temperature of the LBO crystal, which is very beneficial to attain a compact high-stability low-noise single-frequency CW 355 nm UV laser.

The schematic diagram of the designed 355 nm UV laser is presented in Fig. 1. In order to attain a compact single-frequency CW 355 nm laser, a homemade laser diode-pumped

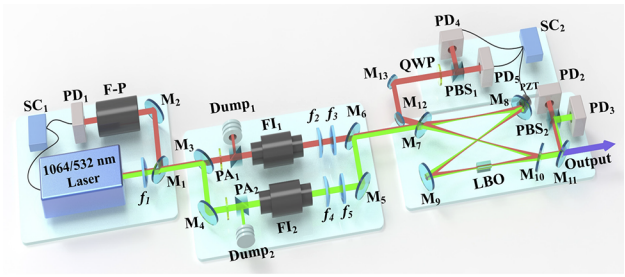

Fig. 1. Schematic diagram of the designed single-frequency CW 355 nm UV laser. SC, servo-controller; PD, photodetector; f, lens; M, mirror; PA, power adjuster; FI, Faraday isolator; PBS, polarization beam splitter; QWP, quarter-wave plate; F–P, Fabry–Perot scanner; PZT, piezoelectric transducer.

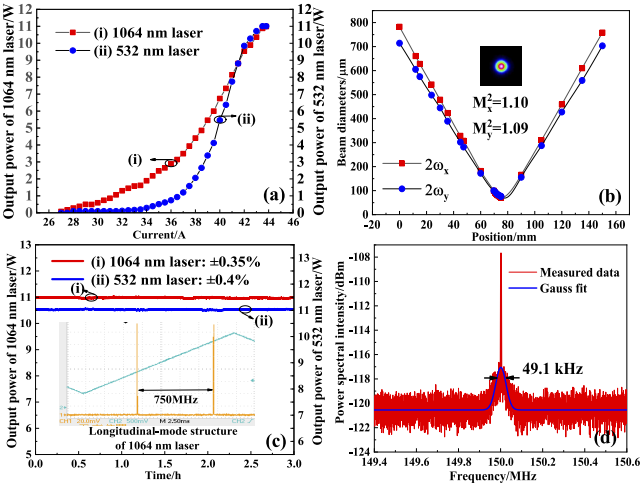

Fig. 2. Output characteristics of the homemade laser source. (a) Output power, (b) beam quality, (c) power stability and longitudinal-mode structure, and (d) linewidth.

single-frequency and intracavity frequency-doubled CW dual-wavelength laser (DPSS FG-VIIIB, Yuguang Co., Ltd.) are firstly built. The intracavity frequency-doubling process can not only ensure the laser to work with single-longitudinal-mode (SLM) operation [13] and achieve the dual-wavelength output [14] but also suppress the laser intensity noise [15] and increase the power stability [16]. The output characteristics of the prepared laser source, including (a) output power, (b) beam quality, (c) power stability, and longitudinal-mode structure as well as (d) linewidth, are depicted in Fig. 2. It is clear that the maximum output powers of the 1064 and 532 nm lasers are as high as 11.02 and 11.05 W, respectively. The measured beam quality values (M^2) of the 532 nm laser in the X direction and Y direction are 1.10 and 1.09, respectively. The power stabilities of the 1064 and 532 nm lasers over 3 h are better than ±0.35% and ±0.4%, respectively, which is benefited from the stable SLM operation. Moreover, the linewidth of the fundamental-wave 1064 nm laser is as narrow as 49.5 kHz, which will be helpful to the achievement of narrow-linewidth 355 nm UV laser.

In addition, the frequency drifts of the fundamental-wave 1064 nm laser and the second-harmonic-wave 532 nm laser are simultaneously monitored by a wavemeter with two channels, and the monitored results are shown in Fig. 3. It can be seen that the frequency drift trend of the 532 nm laser is strictly

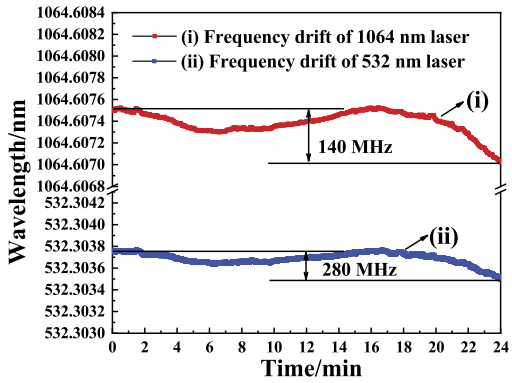

Fig. 3. Frequency drifts of the 1064 and 532 nm lasers.

synchronized to that of the 1064 nm laser, and the frequency drift of the 532 nm laser is 280 MHz in 24 min, which is exactly two times of 140 MHz for the 1064 nm laser. It reveals that there is a strong frequency correlation between the 1064 and 532 nm lasers, which can offer the essential condition for dispersion compensation. Furthermore, this strong frequency correlation also implies that the frequency stability of the single-frequency 355 nm UV laser generated by sum frequency depends heavily on that of the 1064 and 532 nm lasers.

The generated stable 1064 and 532 nm laser beams collimated by a lens f_1 are separated and combined by two dichroic mirrors M_1 and M_6, respectively. In order to prevent optical feedback and precisely adjust the incident powers of 1064 and 532 nm lasers, two optical Faraday isolators (FI_1 and FI_2) and two sets of power adjusters (PA) composed of a half-wave plate (HWP) and a polarization beam splitter (PBS) are inserted into the optical paths, respectively. In order to improve the stability of the achieved 355 nm UV laser, a temperature-controlled and integrated structure cavity body made of quality aviation aluminum is designed and built; all of the cavity mirrors are fixed on the cavity body, which can effectively reduce the change of the mechanical length of the resonator and the disturbance of the air pressure. The sum-frequency cavity is a bow-tie configuration composed of two flat mirrors (M_7 and M_8) and two plano–concave mirrors (M_9 and M_{10}) with the curvature radii of 100 mm. The waist radii between M_9 and M_{10} are 52 and 37 μm for 1064 and 532 nm lasers, respectively. The input coupler M_7 is coated with a partially reflective coating film at 1064 and 532 nm (R = 85% at 1064 nm and R = 90% at 532 nm), which results in the circulating powers of 156 and 194 W for 1064 and 532 nm lasers, respectively. M_8 and M_9 are coated HR films at 1064 and 532 nm. Meanwhile, M_8 is mounted on a piezoelectric transducer (PZT) for the precision-positioning control of the cavity length. The output coupler M_{10} is coated with the HR films at 1064 and 532 nm and the high transmissivity (HT) film at 355 nm. The total optical length of the designed sum-frequency resonator is 495.8 mm. The round trip losses are 3.6% at 1064 nm and 2.9% at 532 nm, respectively, which are obtained by measuring the transmission spectra of the cavity when the input coupler coated with high-reflection films at 1064 and 532 nm is employed.

In order to realize the simultaneous resonance of the incident 1064 and 532 nm lasers and obtain a high-power single-frequency CW 355 nm laser, a temperature-controlled type-I critical-phase-matching LBO crystal with a dimension of $3 \times 3 \times 10$ mm^3 and a phase-matching angle of θ=90°, ϕ=37.1° is employed as the sum-frequency nonlinear crystal as well as

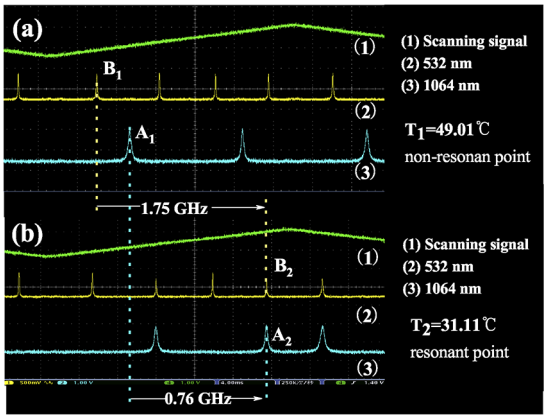

Fig. 4. Transmission peaks of the sum-frequency cavity at (a) non-resonant point and (b) resonant point by scanning the PZT mounted on M_8.

the dispersion-compensated element. The LBO crystal is placed between two plano–concave mirrors M_9 and M_{10} at the strict phase-matching angle of 37.1°. Owing to its temperature insensitivity (0.1°/°C) of phase-matching condition, it is easy to achieve the dispersion compensation for the designed resonator only by scanning the temperature of the LBO crystal. The LBO crystal is placed in a temperature-controlled copper oven with 0.01°C precision. At the same time, two photodiodes (PD_2 and PD_3) are employed to monitor the transmission peaks of 1064 and 532 nm lasers leaked from the sum-frequency cavity, respectively, and the results are illustrated in Fig. 4. It can be seen that the transmission peaks of the 1064 and 532 nm lasers are not overlapped due to the dispersion of the 1064 and 532 nm lasers in the LBO crystal when the temperature of the LBO is set to 49.01°C. As is well-known, the effective optical paths $l(n_i, d)$ in a ring resonator for the oscillating laser beams with different wavelengths should be written as

$$l(n_i, d) = (l - d) + n_i(T)d = k_i\lambda_i, \tag{1}$$

where i stands for the 1064 or 532 nm laser mode. l and d are the geometrical lengths of the built resonator and nonlinear crystal, respectively. n is the refractive index, which is the function of the temperature T. k is the integer and represents the integer times relation between the cavity length and wavelength. In order to realize the dispersion compensation, the relationship between temperature T and refractive index n_i of LBO has to be quantified, which can be analyzed by the following equation:

$$\frac{dn_i}{dT}\Delta T d = \Delta x_i, \tag{2}$$

where dn_i/dT is the temperature-caused index change of LBO and ΔT and Δx_i are the temperature variation and the corresponding change of the optical length caused by the temperature change, respectively.

In the experiment, it is easy to determine the optical length variation Δx_i by scanning the temperature ΔT of the LBO crystal. From Fig. 4, it can be seen that the transmission peak of the 1064 nm laser moves from A_1 to A_2 and that of the 532 nm laser moves from B_1 to B_2 when the temperature is scanned from 49.01 to 31.11°C; the movement amount Δx_1 and Δx_2 can be calculated by the measured movement amount of 0.76 and 1.75 GHz, respectively. Combining the theoretical analysis with the experimental results, the temperature-caused index changes of

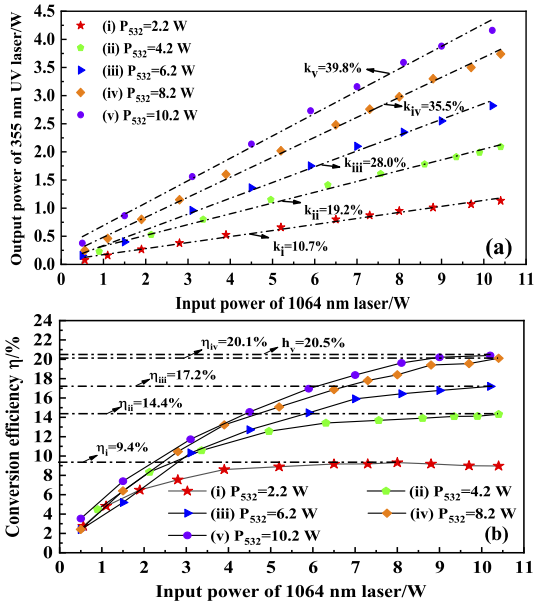

Fig. 5. Output characteristics of the 355 nm UV laser. (a) Output power and (b) conversion efficiency.

LBO at 1064 and 532 nm are successfully determined, which are 7.45×10^{-6} K^{-1} and 8.63×10^{-6} K^{-1}, respectively. The results can provide a valuable reference for our latter doubly resonant point searching.

After the transmission peaks of the 1064 and 532 nm lasers are overlapped, we precisely adjust the angle of the LBO crystal to compensate the small phase-mismatching amount caused by the temperature scanning. Lastly, only finely scan the temperature of the LBO crystal once again to ensure the good overlap of 1064 and 532 nm laser transmission peaks. At this time, if only the sum-frequency cavity is locked to the frequency of the incident 1064 nm laser, the stable single-frequency CW 355 nm UV laser is successfully obtained. Figure 5(a) shows the output power trend of the 355 nm laser with the incident 1064 nm laser at different power levels of the incident 532 nm laser. It is clear that the slopes of the output power curves increase with the increase of the incident 532 nm laser power. When the incident power of the 532 nm laser increases from 2.2 to 10.2 W, the power curve slope of the 355 nm UV laser increases from 10.7 to 39.8%, respectively. When the incident power of the 532 nm laser is 10.2 W, the maximal output power of the 355 nm UV laser is up to 4.2 W. Meanwhile, the total conversion efficiency (ratio of the 355 nm power to the total of incident power) at different 532 nm laser power levels are shown in Fig. 5(b). When the incident power of the 532 nm laser is 2.2 W, the obvious saturation effect of the conversion efficiency is observed at the input power of the 1064 nm laser of 5 W. With the increase of the incident 532 nm laser power, the saturation effect of the conversion efficiency is gradually reduced, and the corresponding maximal conversion efficiency of 20.5% is obtained. The corresponding normalized conversion efficiency is 3.96×10^{-2} W^{-1}. Meanwhile, it is expected that higher output power of the 355 nm laser can be obtained with the further power increase of the incident 1064 and 532 nm lasers.

When the achieved single-frequency 355 nm UV laser works stably with the maximal output power of 4.2 W, the long-term power stability is measured which is shown in Fig. 6(a). The RMS value is 1.4%. Meanwhile, the far-field energy distribution

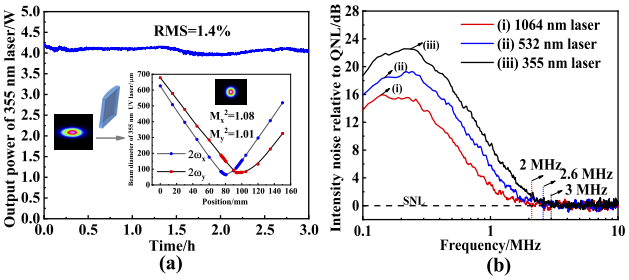

Fig. 6. Output characteristics of the generated 355 nm UV laser. (a) Long-term power stability (the inset is the measured M^2 factors and the spatial beam profile) and (b) intensity noise.

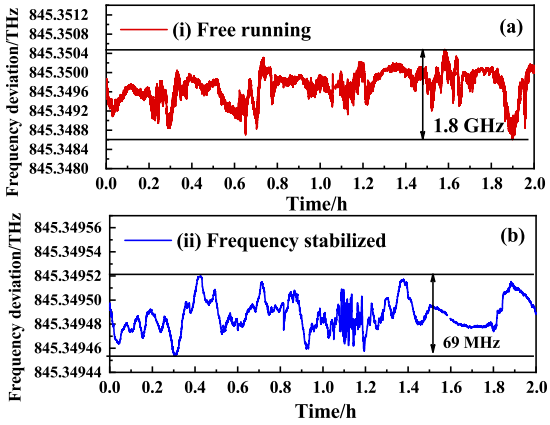

Fig. 7. Long-term frequency drifts of the generated 355 nm UV laser in 2 h. (a) Free running and (b) frequency stabilized.

of the generated 355 nm UV laser is observed. It is found that the 355 nm laser beam is elliptical, which is shown as the left inset in Fig. 6(a), and the ellipticity is 35.5%. In order to improve the beam quality of the 355 nm UV laser, a cylindrical lens in the X direction is used to accomplish the beam shaping. Then an M^2 beam quality analyzer (M2SETVIS, Thorlabs) is employed to measure the beam factors of the shaped 355 nm laser beam; the results are shown in the inset of Fig. 6(a). It is seen that the measured beam quality factors are M_x^2=1.08 and M_y^2=1.01, respectively. Additionally, the intensity noise of the 1064, 532, and generated 355 nm UV lasers are measured in the experiment, respectively, and the results are shown in Fig. 6(b). Curves (i), (ii), and (iii) are the intensity noise spectra of the 1064, 532, and 355 nm lasers relative to the shot noise level (SNL) for the powers of 10.4, 10.2, and 4.2 W, respectively. It is found that the intensity noise of these three wavelength lasers reached the SNL at the frequency of 2, 2.6, and 3 MHz, respectively.

At last, the long-term frequency stability of the generated single-frequency 355 nm UV laser is monitored. When the dual-wavelength laser is in free running, the measured results are shown in Fig. 7(a). It is seen that the frequency drift is 1.8 GHz in 2 h. In order to improve the frequency stability of the generated 355 nm UV laser, a high-stability temperature-controlled Fabry–Perot (F–P) interferometer is specifically designed and employed as the frequency reference of the dual-wavelength laser in the experiment. Benefited from the strong frequency correlation between the 1064 and 532 nm lasers, when the oscillating frequency of the laser source is locked to the designed stable reference cavity, both 1064 and 532 nm lasers with high-frequency stabilities are achieved, which directly lead to a high-stability 355 nm UV laser. Figure 7(b) shows the frequency deviation in 2 h of the generated single-frequency 355 nm UV laser after using the frequency-stabilized system. It is easy to observed that the frequency drift is effectively decreased to 69 MHz in 2 h.

In conclusion, we reported a compact high-power and high-stability all-solid-state CW single-frequency 355 nm UV laser. A homemade all-solid-state dual-wavelength laser was employed to provide frequency-correlated 1064 and 532 nm lasers for the sum-frequency process. Meanwhile, a type-I critical-phase-matching LBO was innovatively used in the external sum-frequency resonator to act as the nonlinear medium as well as the dispersion compensation element to realize a double resonance of 1064 and 532 nm lasers. With the help of the design, the maximal output power of the attained 355 nm UV laser was as high as 4.2 W, and the corresponding conversion efficiency was up to 20.5%. The achieved power stability and beam quality factors are 1.4% (RMS), M_x^2=1.08 and M_y^2=1.01 in the X and Y directions, respectively. The intensity noise of the generated 355 nm UV laser was reached to SNL at the frequency of 3 MHz. Importantly, the long-term frequency drift of the achieved 355 nm UV laser was reduced to 69 MHz with the assistance of our designed high-stability reference cavity. All of the good performances made it possible for the attained all-solid-state CW single-frequency 355 nm UV laser to be well suitable to high-resolution spectroscopy, semiconductor inspection, chip industry, and so on.

Funding. National Natural Science Foundation of China (62027821, 62105192, 62205186); National Key Research and Development Program of China (2022YFC2204003); Research Project Supported by Shanxi Scholarship Council of China (2022-015); Fund for Shanxi "1331 Project" Key Subjects Construction; Scientific and Technological Innovation Program of Higher Education Institutions in Shanxi; First Lab-National Innovation Center (Shanxi) Science and Technology Innovation Project; Special Fund for Science and Technology Innovation Teams of Shanxi Province (202204051002005); Applied Basic Research Project of Shanxi Province, China (202103021221004, 202203021212478, 202203021212481).

Disclosures. The authors declare no conflicts of interest.

Data availability. Data underlying the results presented in this Letter are not publicly available but may be obtained from the authors upon reasonable request.

REFERENCES

1. M. B. Chowdhuri, S. Morita, M. Goto, *et al.*, Rev. Sci. Instrum. **78**, 023501 (2007).
2. Z. Darzynkiewicz, S. Bruno, G. D. Bino, *et al.*, Cytometry **13**, 795 (1992).
3. L. V. Sneppen, A. E. Wiskerke, F. Ariese, *et al.*, Appl. Spectrosc. **60**, 931 (2006).
4. B. Quan, Z. Yao, W. Sun, *et al.*, Microelectron. Eng. **163**, 110 (2016).
5. F. Koch, D. Lehr, and T. Glaser, Proc. SPIE **10448**, 60 (2017).
6. Y. F. Chen, Appl. Phys. B: Lasers Opt. **70**, 475 (2000).
7. Y. Kaneda and S. Kubota, Opt. Lett. **20**, 2204 (1995).
8. Y. Kaneda and S. Kubota, Appl. Opt. **36**, 7766 (1997).
9. C. S. Hsu, J. Y. Lai, D. Y. Wu, *et al.*, Proc. SPIE **11264**, 38 (2020).
10. I. Ricciardi, M. D. Rosa, A. Rocco, *et al.*, Opt. Lett. **34**, 1348 (2009).
11. L. Wang, X. Lin, Y. Yang, *et al.*, Front. Opt. **71**, JW4A.71 (2016).
12. J. Zhang, L. Wang, Y. Li, *et al.*, Opt. Express **20**, 16490 (2012).
13. H. Lu, Y. Guo, and K. Peng, Opt. Lett. **40**, 5196 (2015).
14. C. Zhang, H. Lu, Q. Yin, *et al.*, Appl. Opt. **53**, 6371 (2014).
15. Y. Guo, H. Lu, M. Xu, *et al.*, Opt. Express **26**, 21108 (2018).
16. H. Lu and K. Peng, J. Quantum Opt. **21**, 171 (2015).